Environmental Science Nano

Effect of CeO_2 nanomaterial surface functional groups on tissue and subcellular distribution of Ce in tomato (<I>Solanum lycopersicum)

Journal:	*Environmental Science: Nano*
Manuscript ID	EN-ART-11-2018-001287.R1
Article Type:	Paper
Date Submitted by the Author:	26-Nov-2018
Complete List of Authors:	Li, Jieran; University of Kentucky Department of Plant and Soil Sciences Tappero, Ryan; Brookhaven National Laboratory Acerbo, Alvin; University of Chicago Yan, Hanfei; Brookhaven National Laboratory, Chu, Yong; Brookhaven National Laboratory, National Synchrotron Light Source II Lowry, Gregory ; Carnegie Mellon University, Civil & Environmental Engineering; Center for Environmental Implications of Nanotechnology, Unrine, Jason; University of Kentucky,

Environmental Significance Statement

Terrestrial ecosystems are a major sink for manufactured nanomaterials either through unintentional releases or intentional use in agrochemical formulations. Nanomaterials can be taken up by plants and transferred to herbivores. Recently, it has been shown surface chemistry of manufactured nanoparticles has a profound impact on their uptake and translocation in plants; however, there is a limited understanding of the tissue, cellular and subcellular basis for this. We used a novel hard X-ray nanoprobe with unprecedented spatial resolution (<15 nm) to reveal details about the cellular basis for the effect of surface chemistry on nanoparticle uptake and translocation in plants. This information will greatly enhance our ability to predict how nanomaterial properties influence the uptake, transformations and subsequent trophic transfer of nanomaterials in terrestrial food webs.

Effect of CeO_2 nanomaterial surface functional groups on tissue and subcellular distribution of Ce in tomato (*Solanum lycopersicum*)

Jieran Li[1], Ryan V. Tappero[2], Alvin S. Acerbo[3], Hanfei Yan[2], Yong Chu[2], Gregory V. Lowry[4] and Jason M. Unrine[1,5,*]

1. Department of Toxicology and Cancer Biology, University of Kentucky, Lexington, KY, 40546, USA

2. National Synchrotron Light Source II, Brookhaven National Laboratory, Upton, NY, 11961, USA

3. Consortium for Advanced Radiation Sources, University of Chicago, Chicago, IL, 60637, USA

4. Department of Civil and Environmental Engineering, Carnegie Mellon University, Pittsburgh, PA, 15123, USA

5. Department of Plant and Soil Sciences, University of Kentucky, Lexington, KY, 40546, USA

* Corresponding Author: Jason.Unrine@uky.edu

Abstract

Using recent advances in X-ray microscopy, this study aimed to elucidate mechanisms of uptake, subcellular distribution, and translocation of functionalized CeO_2 MNM (manufactured nanomaterials), having different charges, by tomato plants (*Solanum lycopersicum* cv Micro-Tom). We found that plant growth and Ce concentrations tissues were functions of surface charge and exposure concentration with root to shoot translocation being much greater for negatively charged CeO_2 than positive or neutral CeO_2. Mechanisms of entry into roots and translocation within plants were examined using X-ray nano- and microprobes. There were dramatic differences in the tissue and subcellular distributions of Ce in plant roots exposed to dextran-coated CeO_2 nanoparticles conjugated with positive, neutral and negative functional groups. Positively charged CeO_2 remained mainly bound to the epidermis of the root with little present in the apoplast or cytoplasm. Negatively charged CeO_2 was found in the cytoplasm throughout the root cross section, and negatively charged CeO_2 was found within the apoplast in the cortex and both the apoplast and the cytoplasm in the vasculature. Neutral CeO_2 likely entered through the gaps between epidermal cells being sloughed off during root growth and penetrated deeper into the interior of the roots (vasculature) via a combination of apoplastic and symplastic transport. Evidence of symplastic Ce transport was observed with the neutrally and negatively charged particles. We observed evidence of endocytosis as the mechanism for entry into the symplast allowing for entry into the xylem. This study provides critical information on how particle surface chemistry influences the biodistribution and cellular localization of nanomaterials in plants and is to date the highest resolution X-ray imaging of nanomaterials in plant cells.

Key words: CeO_2 nanoparticles, surface charge, plant uptake, biodistribution

Introduction

In recent years, there has been intense interest in understanding how manufactured nanomaterials (MNM) interact with plants[1-10]. This interest initially developed over concerns about entry of manufactured nanomaterials into terrestrial food chains[11], but more recently, there has been a surge in interest over the use of nanomaterials as targeted fertilizers and pesticides[8 12 13]. Identification of the properties that dictate how MNM interact with plants is crucial to both assessing ecological risks and developing agricultural applications for nanomaterials (phytonanotechnology). Evidence of bioaccumulation of metal and metal oxide MNM by plants is abundant, which usually shows nano-specific effects which differ from treatments with metal ions or bulk materials that are of the same chemical composition [14, 15].

There is still much to be learned about mechanisms behind uptake of nanomaterials in plants and how nanomaterial properties influence these mechanisms. Uptake and translocation of MNM applied to roots requires entry into the xylem. For MNM to move from soil to the xylem, they must cross multiple biological barriers, such as the mucilage and the Casparian strip [16]. The path from the periphery of the root towards the vascular tissue in the center, is critical for translocation of MNM into the leaves and other above ground tissues in a plant. There are three potential routes for movement of water and associated materials from the soil to the xylem: apoplastic, symplastic and transcellular [17]. Many have suggested that the apoplastic route through the extracellular spaces in root is the primary route of transport of MNM to the xylem [18], given that this route is the path of least resistance without entry into the cells; however, the presence of particles within intracellular compartments has also been observed [19-24]. Further, the Casperian strip, a water impermeable barrier located in the endodermis which blocks apoplastic transport, makes it likely that MNM must at some point enter the protoplast of cells to gain entry to the xylem and be transported to aerial portions of the plant. It should be noted, however, the Casparian strip is poorly developed in growing roots, so its effectiveness as a barrier is unclear.

It is widely known that MNM surface chemistry plays a key role in determining the uptake, toxicity, biodistribution and subcellular localization of MNM in organisms[7, 25-27]. The influence of surface chemistry on the mechanisms of uptake and biodistribution in plants has not been well explored and deserves systematic investigation[28]. Such investigations have been previously hampered by a lack of analytical techniques that have the specificity, spatial resolution, and sensitivity required for the task. Fortunately, new tools which combine these capabilities have recently become available at the newest generation of synchrotron light sources. We imaged the subcellular distribution of MNM in plant roots using a novel hard X-ray nanoprobe (HXN) with unprecedented spatial resolution (< 15 nm)[29, 30]. This was complemented by ultra-high sensitivity, spatially resolved X-ray absorption near edge spectroscopy (XANES) to determine speciation of the MNM in fixed plant tissues at ng/g dry mass concentrations.

This study utilizes a set of CeO_2 MNM with identical cores and surface polymers, differing only in functional group substitution and resulting impact on zeta potential. Previous research has demonstrated that these changes in CeO_2 MNM surface chemistry have profound effects on uptake, subcellular localization and toxicity [25, 31]. CeO_2 serves as good model material for studying plant-MNM interactions. It is relatively insoluble in typical plant growth media and can be easily measured and tracked by a number of different imaging and spectroscopic methods.

CeO_2 MNM are among the most widely used nanomaterials found in fuel additives, polishing agents, industrial catalysts, and have recently received interest for use as plant growth promoters in agricultural production [32-35]. In human health research, CeO_2 MNM have received attention both as a potential therapeutic and as a toxicant. The ability of Ce in CeO_2 MNM to undergo reversible transitions between III/IV valence states allows them to behave both as either a pro- or anti-oxidant depending on context [36]. While adverse effects were suggested for CeO_2 MNM in various biological systems [37-39], the impact of key physico-chemical properties affecting the environmental fate and ecotoxicity of these materials such as size and surface coatings have yet to be established [40]. A few in vitro studies have investigated the effects of surface valence state, size, and surface charge on the localization, intracellular trafficking and cytotoxicity of CeO_2 nanoparticles [26, 31, 41]. These studies showed that CeO_2 MNM with neutral polymers localized primarily in the cytoplasm and had minimal toxicity, whereas positively and negatively charged particles were found in lysosomes and caused cytotoxicity [31]. Our previous research demonstrated that positively charged, diethylaminoethyl (DEAE) dextran coated CeO_2 MNM (2-5 nm) were taken up much more efficiently and elicited far greater toxicity in nematodes (*Caenorhabditis elegans*) than neutral dextran coated CeO_2 MNM or negatively charged carboxymethyldextran (CM) coated CeO_2 MNM. We also demonstrated that the macroscopic distribution of neutral and negatively charged CeO_2 NPs in the leaves of wheat plants was different [25].

The objective of this study was to investigate the mechanisms of uptake and biodistribution of a set of well-defined CeO_2 MNM, differing only in surface functional groups and by extension zeta potential, in the model organism tomato (*Solanum lycopersicum* CV Micro Tom). This species is a good model vegetable crop which is easily maintained in the laboratory and has a sequenced genome. This objective required observing the localization and chemical speciation of the materials across spatial scales ranging from the nm scale (10-15 nm) to the mm scale at ng/g concentrations. We hypothesized that surface chemistry would have a profound influence on tissue distribution of CeO_2 MNMs, and that these differences would have a cellular basis. This study has far reaching implications for a general understanding of how surface chemistry influences the behaviors of nanoscale objects taken up by plants. It also provides a powerful demonstration of how material properties can be tailored to control MNM distribution within plants at the tissue and subcellular level for potential phytonanotechnology applications.

Methods

Nanoparticle synthesis and characterization

Dextran coated CeO_2 MNM with a nominal 2-4 nm primary particle diameter (DEX-CeO_2) were synthesized using a previously described procedure[25]. In this study, primary particle diameter was determined by transmission electron microscopy (TEM; JEOL 2010F, Tokyo, Japan) [25]. This dextran coating was then functionalized with diethylaminoethyl groups to confer either a net positive charge (diethylaminoethyl dextran; DEAE-CeO_2), or carboxymethyl groups to confer a net negative charge (carboxymethyl dextran; CM-CeO_2). Details of the synthesis and functionalization of the particles can be found in the Supporting Information (SI). Mean hydrodynamic diameters and electrophoretic mobilities of the MNM treatment suspensions were measured using a Nano-ZS zetasizer (Malvern Instruments, Malvern, United Kingdom) using dynamic light scattering (DLS) and phase analysis light scattering (PALS), respectively. The measurements were made at a suspension concentration of 30 mg Ce/L CeO_2 MNM suspended in 10% Hoagland's solution. The zeta potential was calculated using the Hückel approximation using the Malvern software.

Measurement of dissolution from CeO_2 in media

The nanoparticle treatments were suspended in 10 mL 10% Hoagland's media at the same concentrations used for the experiment (10, 30 and 100 mg/L) and incubated for 24 hours. 5mL of the mixture was filtered through centrifugal devices (Amicon Ultra-4, pore size 3kD equivalent to 1 nm) and the filtrate was collected. To avoid binding of Ce ions to the filter media, which could reduce recovery, the filter was pre-conditioned with 1mM $CuSO_4$ before use. Ultrapure HNO_3 was then added to the filtrate to a final concentration of 0.15 M HNO_3. The unfiltered aliquot was digested by the microwave-assisted method described in the exposure section below. Ce content of the filtrate (5mL) as well as the unfiltered aliquot was analyzed using ICP-MS using previously described methods[25]. The dissolved Ce fraction was calculated as (ng Ce/L in filtrate)/(ng Ce/L in the unfiltered suspension)*100%.

Exposures

Tomato (*Solanum lycopersicum* cv Micro-Tom) plants were germinated on a Phytagel plate (Phytagel, Sigma-Aldritch, St. Louis, MO USA) after which they were transferred and grown hydroponically in 10% Hoagland's solution with a photoperiod of 12 h under fluorescent lights (135 ± 3 μmol photon m^{-2} s^{-1} light intensity) at 25°C. Treatments started with two-week post germination with particles surface-modified with polymer coatings (DEX-CeO_2, DEAE-CeO_2, CM-CeO_2). Exposure media contained high (100 mg/L) medium (30 mg/L) and low (10 mg/L) concentrations of Ce and the exposure duration was 14 d. Fifteen independent biological replicates per treatment were performed. These exposure concentrations were chosen based on the principle that a broad range of sub-lethal concentrations could be tested which caused detectable Ce accumulation in the tissues. The plants were also exposed under the same conditions to various concentrations of $CeCl_3$ to determine the uptake of ionic Ce from the media. Plants were then rinsed with DI water and tissues were collected for determining bulk metal concentrations using ICP-MS and for imaging using synchrotron light sources. Untreated plants were maintained in the same conditions as negative control.

ICP-MS analyses

Freeze-dried plant tissues (roots and shoots collected separately) were digested with 0.75mL concentrated ultra-pure nitric acid and 0.25mL hydrogen peroxide using a microwave system. Samples were then diluted with 5% ultra-pure nitric acid for ICP-MS (Agilent, 7500cx, Santa Clara, CA) analysis. Details of our analytical methods have been described in detail previously[25].

Synchrotron XRF and XANES

Tissues within 1 mm of the tip of the primary roots were dissected with a razor blade, fixed in sodium acetate buffer (pH 7.2) containing 4% glutaraldehyde and 1% formaldehyde and embedded in epoxy resin. Thin sections were cut from the embedded samples at ~1 μm thickness and mounted on a specially made silicon dioxide slide with a platinum finding grid for ultra-high-resolution X-ray fluorescence imaging using the Hard X-ray Nanoprobe (HXN) Beamline 3-ID at NSLS-II, Brookhaven National Laboratory (BNL). NSLS-II is a medium-energy synchrotron operating at 3 GeV. Beamline 3-ID uses multi-layer Laue lenses (MLLs) for final focusing to provide a minimum focus size smaller than 15 nm. For this work, we used various sampling resolutions of 10~100 nanometers per pixel, depending on the resolution and throughput needs for the experiment, albeit for a field-of-view of a few µm. For a complete picture, root tissue cross-sections were imaged at ~1 µm resolution using the GSECARS beamline 13-ID-E at (Advanced Photon Source) APS, Argonne National Laboratory (ANL). The APS is a high energy ring operating at 7 GeV. In addition, spatially-resolved X-ray absorption near edge structure (XANES) spectroscopy was performed at 13-ID-E to interrogate the Ce speciation in root cells. Lastly, the second leaf that emerged from plants in three treatments were clipped intact and mounted with metal-free Kapton tape to aluminum mounts for analysis at Submicron Resolution X-ray Spectroscopy (SRX) Beamline at beamline 5-ID at NSLS-II, BNL. The SRX had a focus size of slightly less than 1 µm. Details are provided in the supplementary information. All three beamlines use undulator insertion devices as the X-ray source.

Spectral Fitting and Image Processing HXN and SRX imaging data

Spectral fitting of HXN and SRX data was performed using the PyXRF spectral fitting program[42]. Briefly, a summed spectrum fit by a user-assisted fitting approach determined global fitting parameters, including the position and peak width of fluorescence peaks, background, pileup and escape peak and Compton and elastic scatter peaks. Then, elemental maps were generated based on the integrated fluorescence intensities determined by the spectral fitting.

Collection of XANES spectra and data reduction

All XANES spectra were plotted and normalized to the region 15-150 eV post edge (the Ce L3 edge at 5726 eV) using Athena[43]. For the root sections, XANES spectra were collected from regions of interest across the entire root and were presented as merged spectra for each treatment. For leaf samples, three XANES spectra were acquired for multiple regions of interest. With the DEAE-CeO_2 and CM-CeO_2 treatments, spectra were merged for all spots examined. We used bulk CeO_2 and $CeCl_3$ as standards for Ce (IV) and Ce (III), respectively. The standards were finely ground to a particle size which corresponded to less than one absorption unit thickness (to avoid self-absorption effects) and mounted on cellulose acetate adhesive tape. Layers of the adhesive tape were stacked until the standards resulted in an approximately 1 absorption unit edge-step.

Statistical analyses

The SAS software package was used for statistical analysis. The data were tested for normality using the Shapiro-Wilk test. The distribution if shoot concentrations of Ce was non-normal hence a non-parametric Kruskal−Wallis one-way ANOVA was used followed by pairwise comparison using the Mann−Whitney U-test. Data points for biomass and root Ce concentrations were found to be normally distributed and were analyzed by one-way ANOVA followed with post-hoc Tukey’s test for pairwise comparisons. Difference with $p<0.05$ was considered to be statistically significant. We used 15 replicates per treatment and all were included in statistical analyses.

Results and Discussion

Nanoparticle synthesis and characterization.

We utilized a set of CeO_2 MNM that differed only by zeta potential, as conferred by substituting different functional groups on their surface polymers. The synthesis and characterization of these MNM has been described previously[25]. We synthesized dextran coated CeO_2 MNM (DEX-CeO2) and then substituted diethylaminoethyl groups (DEAE) into the dextran to confer positive charge or carboxymethyl groups, (CM) to confer negative charge. The primary crystallite size of the CeO_2 cores, as measured by transmission emission microscope (TEM), ranged from 2-4 nm. Dynamic light scattering (DLS) and phase analysis light scattering (PALS) showed that the hydrodynamic diameters of the particles were similar in the exposure media (ranging from 16-22 nm), but the apparent zeta potentials differed as expected (Table 1). The zeta potentials were +13, -3 and -15 for the DEAE-CeO_2, DEX-CeO_2, and CM-CeO_2 treatments, respectively. Dissolution of the CeO_2, as determined by ultrafiltration (1 nm nominal pore size) and inductively coupled plasma mass spectrometry (ICP- MS), showed that negligible dissolution (<0.31%) occurred in the exposure media for all three particle types over the timescales of the experiments (Table 1).

Toxicity

One-week after germination, tomato seedlings were transferred from germination plates to exposure solutions containing 10, 30, and 100 mg Ce/L in the forms of DEX-CeO_2, DEAE and CM-CeO_2 for 14 d. Compared to control, tissue dry mass was significantly reduced in particle-treated groups for both roots and shoots after two weeks of exposure (Fig 1). Positively charged DEAE-CeO_2 treatment caused significantly greater growth inhibition than the other two treatment groups. Light microscopy of the root tips from the highest exposure concentrations revealed cell damage (Fig 2). Lesions resulting from cell death can be clearly seen in the root tip regions of plants in the DEAE-CeO_2 treatment. Cell shrinkage was observed in roots from the

DEX treatment. Such cellular injury can severely hamper the function of the roots, such as the ability to absorb and transport minerals, which might explain the chlorotic symptoms observed in the leaves (Fig. S1).

In contrast to our observations, previous studies have shown moderate toxicity for CeO_2 NPs in various plant species [44-46]. Sometimes, even beneficial effects were noted for these particles on seed germination and seedling growth [45]. However, particles used in these studies were without surface coatings and considerably larger in size (>20 nm) as compared to particles used in this study (2-4 nm) [44-46]. The increased toxicity of our materials relative to those used in previous studies may relate to increased reactivity of CeO_2 particles of <10 nm in diameter, enhanced colloidal stability of polymer coated CeO_2 and/or the charged functional groups, particularly the positively charged DEAE groups.

Tissue distribution

Root Ce concentrations were drastically different among the treatments (Fig 3), with the DEAE-CeO_2 (positive) and DEX-CeO_2 (neutral) treatments having much higher Ce concentrations than CM-CeO_2 (negative). The outermost surface of roots is a mucilage layer which consists of polysaccharides and proteinaceous substances. Under typical soil pH values, this layer gives the root a negatively charged surface, which would therefore have a greater affinity for neutral and positively charged MNM than negatively charged MNM. This result is consistent with a similar trend of root association as influenced by surface coating and charge noticed in previous studies [47-49], suggesting a consistent mechanism governing the interaction. Our previous study with the same particles used in this study revealed a similar trend of tissue distribution and similar root masses of Ce within wheat plants (*Triticum aestivum*) exposed for up to 34h [50].

Analysis of the shoot tissues revealed that accumulation in the roots did not predict the extent to which Ce was translocated to the aerial part of the plants. Despite having lower root concentration, a greater quantity of the CM-CeO_2 (negatively charged) coated MNM were translocated to the shoots than the other two treatments (Fig. 3C). This, together with the fact that only a small fraction of Ce was translocated from the roots to the shoots, indicates that the majority of Ce associated with the root tissue did not enter the xylem, which is the only route by which materials are carried from root to shoot.

We also examined the consequences of exposure to ionic Ce using dissolved $CeCl_3$ (Fig S2). Growth retardation from the ionic Ce (III) treatment was insignificant when exposure concentrations were below 5 mg Ce/L. Given the low dissolution rate of CeO_2 in exposure media shown in Table 1, the toxicity and Ce bioaccumulation are not likely due to uptake of ions from bulk solution, although dissolution at the root surface is possible. Furthermore, under the highest $CeCl_3$ exposure concentration (15 mg Ce/L), which was toxic to the plants, less Ce was translocated to the shoots, whereas for the particle treatments, translocation rates remained high even with plants suffering from the most severe toxicity (DEAE-CeO_2-treated). Given that the Hoagland's medium contains phosphate, it is possible that $CePO_4$ precipitate formed in the $CeCl_3$ treatment, limiting uptake.

Subcellular distribution and speciation of Ce in root tips

Numerous previous studies have demonstrated that a variety of plant species take up various types of MNM. However, the mechanism of uptake has remained enigmatic. A recent study investigating exposure of alfalfa (*Medicago sativa*) to Ag and Ag_2S nanoparticles indicated that the root tip is the site where nanoparticles likely enter the plant [18]. Data for the overall distribution of Ce in cross sections of the root tip was obtained at ~1 μm resolution showed that distributions of Ce in the tissue are different for the three treatments. Ce appears to be co-localized with the cell wall/cell membrane boundaries in DEX-CeO_2-treated root at this resolution (Fig. 4 A, B). In the CM-CeO_2-treated root, Ce was found almost across the entire root cross section. Scattered hotspots were visible as well as regions with a more diffuse distribution (Fig. 4 F,G). For the DEAE-CeO_2-treated root (positive charge), Ce was found primarily on the epidermis, with little in the interior of the root (Fig. 4 K,L).

Images showing the cellular and subcellular distribution of Ce within the root tips using the HXN are shown in Fig 4 C, D, E, H, I, J, M and Fig. S4. These images entry of Ce into plant roots at the cellular level. Clearly observed in the DEX-CeO_2 (neutral) treatment, is Ce present within spaces between the epidermal cells that are partially separated from the epidermis, presumably as a result as cells are being shed from the epidermis during root tip growth (Fig. 4C, S4). The presence of Ce in the apoplastic spaces between cells (Fig 4D, E and Fig. S4), which are approximate 100-200 nm across, suggests that movement through these spaces is the route of passage from the epidermis to the vascular tissue. The presence of intracellular Ce hotspots in the cytoplasm of cells near the vascular bundle in the center of the root suggests that Ce was actively internalized by the cells within this region (Fig.4E). Within the stele itself, cells appear to show Ce both within the apoplast and throughout the cytoplasm within intracellular vesicles which are likely endosomes (Fig 4E and Fig 5). The Casparian strip is a barrier in the endodermis that prevents mass transfer from the cortex into the xylem. It has been an open question as to how particles traverse this barrier. One hypothesis was that they move through poorly developed regions of the Casparian strip in the root tip. Without completely ruling out that hypothesis, we conclude based on the evidence presented here that the particles are also endocytosed within the inner regions of the cortex and transferred across the endodermis symplastically.

XANES spectroscopy is very useful in distinguishing between the two primary oxidation states of Ce (Ce(III) and Ce(IV)), with Ce(III) producing a solitary absorption peak or "white line" at 5722 keV, and Ce(IV) producing two peaks at 5725 and 5732 keV. The particles mostly consist of Ce (IV) as-synthesized, although a small percentage of the atoms are in the Ce (III) state due to oxygen vacancies as shown in our previous work[51]. An important question is whether this material is intact DEX-CeO_2 or transformation products. We conclude that at least a portion of this material is intact CeO_2. The proportion of Ce (IV) in the epidermis, cortex, and vasculature 47, 32 and 36 percent, respectively (Fig 6). Given that the percentage of Ce (IV) is similar in the cortex, which where Ce was primarily located in the apoplastic space, was similar to the vasculature, where Ce was primarily found in the cytoplasm, it is likely that both intact CeO_2 and transformation products were internalized into cells. However, Fig 5 clearly shows, that if present, these transformation products must have been nanoscale or smaller, given that the size of the Ce hotspots in the cytoplasm was less than 20 nm. $CePO_4$ particles seen in previous studies as transformation products (Zhang et al.[52]; Rui et al.[53],) are typically larger than this. Dextran-coated CeO_2 particles within this size range (<5 nm) can accommodate Ce (III) atoms within their crystal structure and these atoms can reversibly transition between the +III and +IV oxidation states (Perez et al.[54]; Graham et al.[51]), so it is possible that these <20 nm hotspots contain CeO_2 particles with a large percentage of oxygen vacancies on the surface giving them a greater percentage of Ce (III)[51]. The presence of Ce ions bound to macromolecules is unlikely as they would likely have had a much more diffuse distribution as has been seen with Cu ions in tissues versus Cu oxides [55].

A previous study suggested that the primary site of biotransformation is on the surface of the epidermis[53]. Given that the percentage of Ce (IV) was similar in epidermis and the vasculature, we cannot rule this out. It is important to note that the particles used in our study are far smaller at 2-4 nm, than particles used in this previous study[53] which used 25 nm particles, and are likely more readily reduced[51,54], so they may behave differently intracellularly. In our previous study, differences in Ce(IV)/Ce(III) ratios were observed for hydroponic exposures to wheat plants, with a higher Ce(IV)/Ce(III) ratio being observed in areas with greater total Ce concentration, and a lower Ce(IV)/Ce(III) ratio observed in areas with less total Ce [48]. This suggests differential transport of transformation products within the tissues, relative to intact materials.

A very different distribution pattern emerged in the CM-CeO_2 (negative) treatment (Fig 4G). In addition to the apoplast, Ce was observed in the cytoplasm throughout the cells in the cortex (Fig 4H&I). High resolution HXN imaging clearly identified multiple circular/spherical structures of around 100 nm in diameter within the cells containing Ce (Fig.4 J), again suggestive of the presence of particles within endosomes. Thus, it appears that the negatively charged particles are more actively endocytosed within all regions of the cortex and exist in both the symplastic and apoplastic compartments of the root tissue. This suggests to us that the cortical cells preferentially endocytose negatively charged particles. It is possible that endocytosis of the DEX-CeO_2 particles began within the inner regions of the cortex as they gained a negative charge due to the formation of a protein corona. It has been shown that acquisition of a protein corona, or surface coating of proteins, confers a net negative charge to nanoparticles with a wide variety of initial surface chemistries [56, 57]. Alternatively, endocytosis is less charge-specific within the inner cortex.

The percentage of Ce (III) in CM-CeO_2 treated root tissue decreased from the epidermis (54%) to the cortex (49 %) and vasculature (24%) (Fig. 6). This suggests that untransformed particles were preferentially transported to the cortex from the epidermis, and it does tend to support the hypothesis that the majority of transformation of the CM-CeO_2 particles occurred in the epidermis.

For the DEAE-CeO_2 (positive) treatment, the root was completely coated with a thick (>1µm) layer containing high concentrations of Ce (Fig 4 K,L, and M), which correlates with the high bulk Ce concentration detected in roots by ICP-MS relative to the other two treatments (Fig 3). Low concentrations of Ce within the cortex and vascular tissues made it impossible to discern the tissue and subcellular level distribution of the DEAE-CeO_2 particles. This explains the relatively poor translocation efficiency observed for the DEAE-CeO_2 treatment. It remains unclear whether the necrosis in root tissue observed in this treatment resulted from impairment of water or nutrient uptake through the root hairs and epidermis or was primarily caused by internalized DEAE-CeO_2 particles, which only account for a small fraction of the observed Ce. Necrosis in the root tissue is likely a significant cause of observed decreased growth and foliar symptoms. Our previous studies of the same materials with the nematode *C. elegans* found that the DEAE-

CeO_2 particles were several orders of magnitude more toxic than the CM-CeO_2 or DEX-CeO_2 particles, even after factoring in differences in bioavailability among the particle types [25, 58].

The percentage of Ce (III) was slightly higher in the cortex (34%) than the epidermis (22%) for DEAE-CeO_2 treated plants (Fig. 6). This suggests two possibilities, either CeO_2 continued to be transformed within the cortex, or transformed particles were preferentially transported to the cortex from the epidermis. Although preferential transport of transformation products seems unlikely given their larger size, we cannot rule out this hypothesis.

Cerium distribution and speciation within leaf tissue

Because of the low concentrations of Ce found within the shoots, and even lower concentrations in the leaf tissue itself (Fig S3), we required lower detection limits for imaging than were possible at HXN. We utilized the Submicron Resolution X-ray Spectroscopy (SRX) Beamline at NSLS-II which enabled micron-scale imaging and XANES spectroscopy at low to sub- mg/kg Ce concentrations. Again, surface charge greatly affected the distribution of Ce within leaves (Fig.7). In the CM-CeO_2 treatment, the majority of the Ce was found within the vascular tissue in relatively large foci with few smaller foci within the mesophyll. The Ce in the DEX-CeO_2 and DEAE-CeO_2 treatment was distributed primarily as small foci. XANES spectra collected at the foci from the DEAE-CeO_2 leaf sample, which located primarily in the mesophyll, indicated the predominance of Ce (IV) (Fig 7D). In contrast, almost all the Ce regions in the CM-CeO_2 leaf were shown to contain the reduced form, Ce (III). For the DEX-CeO_2 treatment, Ce (III) was still the major form in the veins while small spots in the mesophyll produced characteristic Ce (IV) peaks.

Dissolved Ce^{3+} is likely released through reductive dissolution of CeO_2 and may precipitate as relatively large Ce (III) phosphate crystallites. These large elongated hexagonal cerium phosphate crystals have been previously observed in the apoplast of cucumber plants exposed to CeO_2 MNM [52]. While Ce L-edge XANES is not capable of discriminating between different Ce (III) compounds, Zhang et al.[52], used FTIR spectroscopy to confirm that these crystals, which they observed using TEM, were $CePO_4$. The spatially resolved XANES spectroscopy presented here also show that the untransformed CeO_2 is accumulated primarily within the mesophyll, while Ce (III) accumulated within the vasculature (Fig 7). This is most clearly shown for the DEX-CeO_2 treatment where merged spectra from the mesophyll are 73% Ce (IV), while the veins contain only 46% Ce (IV). These very small Ce (IV) hotspots may be intact particles while the larger elongated structures observed in the veins may be the hexagonal $CePO_4$ structures observed by Zhang et al.[52].

Conclusion

Surface functionalization had a profound influence on the uptake, tissue and subcellular distribution CeO_2 MNM in the plants. Endocytosis also appears to be more efficient for negatively charged CeO_2 than positively charged CeO_2 or neutral CeO_2 in the plant root tip cells. This likely explains the dramatic difference in translocation of these differentially charged CeO_2 MNM. When MNM age in natural soil, they are likely to ultimately gain a coating of natural organic matter, conferring a net negative charge. This may ultimately enhance their translocation to leaves regardless of initial surface chemistry. Finally, the differential tissue and cellular distribution as a function of particle surface chemistry suggests that targeted, MNM-mediated delivery of agrochemicals to different biological compartments within the plant is possible at both the tissue and subcellular levels.

Supporting Information

Supporting Information is available online

Acknowledgements

This material is based upon work supported by the National Science Foundation under Grants 1530594 and 1266252. This research also used the Hard X-ray Nanoprobe (HXN) Beamline at 3-ID and the Submicron Resolution X-ray Spectroscopy (SRX) Beamline at 5-ID National Synchrotron Light Source II, a U.S. Department of Energy (DOE) Office of Science User Facility operated for the DOE Office of Science by Brookhaven National Laboratory under Contract No. DE-SC0012704. Portions of this work were performed at GSECARS (The University of Chicago, Sector 13), Advanced Photon Source (APS), Argonne National Laboratory. GSECARS is supported by the National Science Foundation – Earth Sciences (EAR-1128799) and Department of Energy – Geosciences (DE-FG02-94ER14466). APS facility is supported by DOE under Contract No. DE-AC02-06CH11357. The authors acknowledge Y-C. Chen-Wiegert, L. Li, J. Thieme, W. Rao, J. Begley, S. Sutton, M. Newville, and A. Lanzirotti.

Conflict of Interest

The authors declare that there are no competing interests associated with this manuscript.

References

1. D. Lin and B. Xing, Phytotoxicity of nanoparticles: inhibition of seed germination and root growth, *Environ Pollut*, 2007, **150**, 243-250.

2. F. Torney, B. G. Trewyn, V. S. Lin and K. Wang, Mesoporous silica nanoparticles deliver DNA and chemicals into plants, *Nat Nanotechnol*, 2007, **2**, 295-300.

3. W. M. Lee, Y. J. An, H. Yoon and H. S. Kweon, Toxicity and bioavailability of copper nanoparticles to the terrestrial plants mung bean (Phaseolus radiatus) and wheat (Triticum aestivum): plant agar test for water-insoluble nanoparticles, *Environ Toxicol Chem*, 2008, **27**, 1915-1921.

4. D. Lin and B. Xing, Root uptake and phytotoxicity of ZnO nanoparticles, *Environ Sci Technol*, 2008, **42**, 5580-5585.

5. E. Corredor, P. S. Testillano, M. J. Coronado, P. Gonzalez-Melendi, R. Fernandez-Pacheco, C. Marquina, M. R. Ibarra, J. M. de la Fuente, D. Rubiales, A. Perez-De-Luque and M. C. Risueno, Nanoparticle penetration and transport in living pumpkin plants: in situ subcellular identification, *BMC Plant Biol*, 2009, **9**.

6. E. Wild and K. C. Jones, Novel method for the direct visualization of in vivo nanomaterials and chemical interactions in plants, *Environ Sci Technol*, 2009, **43**, 5290-5294.

7. K. Birbaum, R. Brogioli, M. Schellenberg, E. Martinoia, W. J. Stark, D. Gunther and L. K.

Limbach, No evidence for cerium dioxide nanoparticle translocation in maize plants, *Environ Sci Technol*, 2010, **44**, 8718-8723.

8. R. Nair, S. H. Varghese, B. G. Nair, T. Maekawa, Y. Yoshida and D. S. Kumar, Nanoparticulate material delivery to plants, *Plant Sci*, 2010, **179**, 154-163.

9. A. Mukherjee, S. Bandyopadhyay, C. Rico, L. J. Zhao, J. R. Peralta-Videa and J. L. Gardea-Torresdey, ZnO nanoparticle induced phytotoxicity and differential anti-oxidative stress in green peas (*Pisum sativum* L.) cultivated in soil, *Abstr Pap Am Chem S*, 2013, **246**.

10. J. Hong, C. M. Rico, L. Zhao, A. S. Adeleye, A. A. Keller, J. R. Peralta-Videa and J. L. Gardea-Torresdey, Toxic effects of copper-based nanoparticles or compounds to lettuce (*Lactuca sativa*) and alfalfa (*Medicago sativa*), *Environ Sci Proc & Imp*, 2015, **17**, 177-185.

11. J. D. Judy, J. M. Unrine and P. M. Bertsch, Evidence for biomagnification of gold nanoparticles within a terrestrial food chain, *Environ Sci Technol*, 2011, **45**, 776-781.

12. L. E. Wang P, Zhao FJ, Kopittke PM., Nanotechnology: A new opportunity in plant sciences, *Trends Plant Sci*, 2016, **21**, 699-712.

13. S. M. Rodrigues, P. Demokritou, N. Dokoozlian, C. O. Hendren, B. Karn, M. S. Mauter, O. A. Sadik, M. Safarpour, J. M. Unrine, J. Viers, P. Welle, J. C. White, M. R. Wiesner and G. V. Lowry, Nanotechnology for sustainable food production: promising opportunities and scientific challenges, *Environ Sci Nano*, 2017, DOI: 10.1039/c6en00573j.

14. S. J. Klaine, P. J. Alvarez, G. E. Batley, T. F. Fernandes, R. D. Handy, D. Y. Lyon, S. Mahendra, M. J.McLaughlin and J. R. Lead, Nanomaterials in the environment: behavior, fate, bioavailability, and effects, *Environ Toxicol Chem*, 2008, **27**, 1825-1851.

15. P. Miralles, T. L. Church and A. T. Harris, Toxicity, Uptake, and Translocation of

Engineered Nanomaterials in Vascular plants, *Environ Sci Technol*, 2012, **46**, 9224-9239.

16. K. J. Dietz and S. Herth, Plant nanotoxicology, *Trends Plant Sci*, 2011, **16**, 582-589.

17. E. Steudle, Review article. How does water get through roots?, *J Exp Bot*, 1998, **49**, 775-788.

18. J. Stegemeier, F. Schwab, B. Colman, S. Webb, M. Newville, A. Lanzirotti, C. WInkler, M. Wiesner and L. GV, Speciation Matters: Bioavailability of Silver and Silver Sulfide Nanoparticles to Alfalfa (*Medicago sativa*). *Environ Sci Technol*, 2015, **49**, 8451-8460.

19. P. Wang, E. Lombi, F. J. Zhao and P. M. Kopittke, Nanotechnology: A New Opportunity in Plant Sciences, *Trends Plant Sci*, 2016, **21**, 699-712.

20. J. Geisler-Lee, Q. Wang, Y. Yao, W. Zhang, M. Geisler, K. Li, Y. Huang, Y. Chen, A. Kolmakov and X. Ma, Phytotoxicity, accumulation and transport of silver nanoparticles by *Arabidopsis thaliana*, *Nanotoxicology*, 2013, **7**, 323-337.

21. D. Sun, H. I. Hussain, Z. Yi, R. Siegele, T. Cresswell, L. Kong and D. M. Cahill, Uptake and cellular distribution, in four plant species, of fluorescently labeled mesoporous silica nanoparticles, *Plant Cell Rep*, 2014, **33**, 1389-1402.

22. Y. Ma, X. He, P. Zhang, Z. Zhang, Guo and T. Z, R, et al. , Phytotoxicity and biotransformation of La2O3 nanoparticles in a terrestrial plant cucumber (*Cucumis sativus*). , *Nanotoxicology* 2011, **5**, 743-753.

23. E. Corredor, P. S. Testillano, M. J. Coronado, P. Gonzalez-Melendi, R. Fernandez-Pacheco, C. Marquina, M. R. Ibarra, J. M. de la Fuente, D. Rubiales, A. Perez-de-Luque and M. C. Risueno, Nanoparticle penetration and transport in living pumpkin plants: in situ subcellular identification, *BMC Plant Biol*, 2009, **9**, 45.

24. T. Aubert, A. Burel, M. A. Esnault, S. Cordier, F. Grasset and F. Cabello-Hurtado, Root uptake and phytotoxicity of nanosized molybdenum octahedral clusters, *J Hazard Mater*, 2012,

219-220, 111-118.

25. B. Collin, E. Oostveen, O. V. Tsyusko and J. M. Unrine, Influence of natural organic matter and surface charge on the toxicity and bioaccumulation of functionalized ceria nanoparticles in *Caenorhabditis elegans*, *Environ Sci Technol*, 2014, **48**, 1280-1289.

26. G. Pulido-Reyes, I. Rodea-Palomares, S. Das, T. S. Sakthivel, F. Leganes, R. Rosal, S. Seal and F. Fernandez-Pinas, Untangling the biological effects of cerium oxide nanoparticles: the role of surface valence states, *Sci Rep*, 2015, **5**, 15613.

27. C. M. Goodman, C. D. McCusker, T. Yilmaz and V. M. Rotello, Toxicity of gold nanoparticles functionalized with cationic and anionic side chains, *Bioconjug Chem*, 2004, **15**, 897-900.

28. J. Judy and P. Bertsch, Bioavailability, toxicity, and fate of manufactured nanomaterials in terrestrial ecosystems, *Adv Agron*, 2014, **123**, 1-64.

29. X. Huang, H. Yan, E. Nazaretski, R. Conley, N. Bouet, J. Zhou, K. Lauer, L. Li, D. Eom, D. Legnini, R. Harder, I. K. Robinson and Y. S. Chu, 11 nm hard X-ray focus from a large-aperture multilayer Laue lens, *Sci Rep*, 2013, **3**, 3562.

30. E. Nazaretski, H. Yan, K. Lauer, N. Bouet, X. Huang, W. Xu, J. Zhou, D. Shu, Y. Hwu and Y. S. Chu, Design and performance of an X-ray scanning microscope at the Hard X-ray Nanoprobe beamline of NSLS-II, *J Synchr Rad*, 2017, **24**, 1113-1119.

31. A. Asati, S. Santra, C. Kaittanis and J. M. Perez, Surface-charge-dependent cell localization and cytotoxicity of cerium oxide nanoparticles, *ACS Nano*, 2010, **4**, 5321-5331.

32. K. Reed, Exploring the properties and applications of nanoceria: is there still plenty of room at the bottom? , *Environ Sci Nano*, 2014, **1**, 390-405.

33. X. Pang, D. Li and A. Peng, Application of rare-earth elements in the agriculture of China

and its environmental behavior in soil, *Environ Sci Pollut Res Int*, 2002, **9**, 143-148.

34. T. Yu, Y. I. Park, M. C. Kang, J. Joo, J. K. Park, H. Y. Won, J. J. Kim and T. Hyeon, Large-scale synthesis of water dispersible ceria nanocrystals by a simple sol-gel process and their use as a chemical mechanical planarization slurry, *Eur J Inorg Chem*, 2008, **6**, 855-858.

35. A. Trovarelli, C. de Leitenburg, M. Boaro and G. Dolcetti, The utilization of ceria in industrial catalysis, *Catal Today* 1990, **50**, 353-367.

36. I. Celardo, J. Z. Pedersen, E. Traversa and L. Ghibelli, Pharmacological potential of cerium oxide nanoparticles, *Nanoscale*, 2011, **3**, 1411-1420.

37. A. Thill, O. Zeyons, O. Spalla, F. Chauvat, J. Rose, M. Auffan and A. M. Flank, Cytotoxicity of CeO_2 nanoparticles for Escherichia coli. Physico-chemical insight of the cytotoxicity mechanism, *Environ Sci Technol*, 2006, **40**, 6151-6156.

38. H. Zhang, X. He, Z. Zhang, P. Zhang, Y. Li, Y. Ma, Y. Kuang, Y. Zhao and Z. Chai, Nano-CeO_2 exhibits adverse effects at environmental relevant concentrations, *Enviro Sci Techno*l 2011, **45**, 3725+3730.

39. K. Van Hoecke, J. T. Quik, J. Mankiewicz-Boczek, K. A. De Schamphelaere, A. Elsaesser, P. Van der Meeren, C. Barnes, G. McKerr, C. V. Howard, D. Van de Meent, K. Rydzynski, K. A. Dawson, A. Salvati, A. Lesniak, I. Lynch, G. Silversmit, B. De Samber, L. Vincze and C. R. Janssen, Fate and effects of CeO_2 nanoparticles in aquatic ecotoxicity tests, *Environ Sci Technol*, 2009, **43**, 4537-4546.

40. A. S. Karakoti, P. Munusamy, K. Hostetler, V. Kodali, S. Kuchibhatla, G. Orr, J. G. Pounds, J. G. Teeguarden, B. D. Thrall and D. R. Baer, Preparation and characterization challenges to understanding environmental and biological impacts of ceria nanoparticles, *Surf Interface Anal*, 2012, **44**, 882-889.

41. J. Rejman, V. Oberle, I. S. Zuhorn and D. Hoekstra, Size-dependent internalization of particles via the pathways of clathrin- and caveolae-mediated endocytosis, *Biochem J*, 2004, **377**, 159-169.

42. L. Li, H. Yan, W. Xu, D. Yu, A. Heroux, W.-K. Lee, S. Campbell and Y. Chu, Python-based X-ray fluorescence analysis package, *Proc. SPIE 10389, X-ray Nanoimaging: Instruments and Methods III*, 2017, DOI: Doi:10.117/12.2272585.

43. B. Ravel and M. Newville, Athena, Artemis, Hephaestus: data analysis for X-ray absorption spectroscopy using IFEFFIT, *J Synchrotron Rad*, 2005, **12**, 537-541.

44. C. M. Rico, J. Hong, M. Morales, L. Zho, A. Barrios, J.-Y. Zhang, J. R. Peralta-Videa and J. L. Gardea-Torresdey, Effect of Cerium Oxide Nanoparticles on Rice: A Study Involving the Antioxidant Defense System and In Vivo Fluorescence Imaging, *Environ Sci Technol*, 2013, **47**, 5635-5642.

45. P. Thomas, D. Carpenter, C. Boutin and J. Allison, Rare earth elements (REEs): Effects on germination and growth of selected crop and native plant species, *Chemosphere*, 2014, **78**, 273-279.

46. Y. Ma, L. Kuang, X. He, W. Bai, Y. Ding, Z. Zhang, Y. Zhao and Z. Chai, Effects of rare earth oxide nanoparticles on root elongation of plants, *Chemosphere* 2010, **78**, 273-279.

47. J. Koelmel, T. Leland, H. Wang, D. Amarasiriwardena and B. Xing, Investigation of gold nanoparticles uptake and their tissue level distribution in rice plants by laser ablation-inductively coupled-mass spectrometry, *Environ Pollut,* 2013, **174**, 222-228.

48. H. Li, X. Ye, X. Guo, Z. Geng and G. Wang, Effects of surface ligands on the uptake and transport of gold nanoparticles in rice and tomato, *J Hazard Mater*, 2016, **314**, 188-196.

49. J. Wang, Y. Yang, H. Zhu, J. Braam, J. L. Schnoor and P. J. Alvarez, Uptake, translocation,

and transformation of quantum dots with cationic versus anionic coatings by *Populus deltoides* x *nigra* cuttings, *Environ Sci Technol*, 2014, **48**, 6754-6762.

50. E. Spielman-Sun, E. Lombi, E. Donner, D. Howard, J. M. Unrine and G. V. Lowry, Impact of Surface Charge on Cerium Oxide Nanoparticle Uptake and Translocation by Wheat (*Triticum aestivum*), *Environ Sci Technol*, 2017, **51**, 7361-7368.

51. M. Graham Uschi, T. Tseng Michael, B. Jasinski Jacek, A. Yokel Robert, M. Unrine Jason, H. Davis Burtron, K. Dozier Alan, S. Hardas Sarita, R. Sultana, A. Grulke Eric and D. A. Butterfield, In Vivo Processing of Ceria Nanoparticles inside Liver: Impact on Free-Radical Scavenging Activity and Oxidative Stress, *ChemPlusChem*, 2014, **79**, 1083-1088.

52. P. Zhang, Y. Ma, Z. Zhang, X. He, J. Zhang, Z. Guo, R. Tai, Y. Zhao and Z. Chai, Biotransformation of Ceria Nanoparticles in Cucumber Plants, *ACS Nano*, 2012, **6**, 9943-9950.

53. Y. Rui, P. Zhang, Y. Zhang, Y. Ma, X. He, X. Gui, Y. Li, J. Zhang, L. Zheng, S. Chu, Z. Guo, Z. Chai, Y. Zhao and Z. Zhang, Transformation of ceria nanoparticles in cucumber plants is influenced by phosphate, *Environ Poll*, 2015, **198**, 8-14.

54. J. M. Perez, A. Asati, S. Nath and C. Kaittanis, Synthesis of biocompatible dextran-coated nanoceria with pH-dependent antioxidant properties, *Small*, 2008, **4**, 552-556.

55. J. Unrine, O. Tsyusko, S. Hunyadi, J. Judy and P. Bertsch, Effects of particle size on chemical speciation and bioavailability of Cu to earthworms exposed to Cu nanoparticles, *J Environ Qual*, 2010, **39**, 1942-1953.

56. CD Walkey, F Song, R Liu, H Guo, DWH Olsen, Y Cohen, A Emili, and WCW Chan, Protein Corona Fingerprinting Predicts the Cellular Interaction of Gold and Silver Nanoparticles, *ACS Nano*, 2014, **8**, 439-2455.

57. M. Lundqvist, J. Stigler, T. Cedervall, T. Berggard, M. Flanagan, I. Lynch, G. Eliaz and K.

Dawson, The Evolution of the Protein Corona around Nanoparticles: A Test Study, *ACS Nano*, 2011, **5**, 7503-7509.

58. D. A. Arndt, E. K. Oostveen, J. Triplett, D. Allan Butterfield, O. V. Tsyusko, B. Collin, D. L. Starnes, J. Cai, J. B. Klein, R. Nass and J. M. Unrine, The role of charge in the toxicity of polymer-coated cerium oxide nanomaterials to *Caenorhabditis elegans*, *Comp Biochem Physiol C: Toxicol Pharmacol*, 2017, **201**, 1-10.

Table 1. Size distribution, zeta potential, and dissolution of polymer coated CeO_2 nanoparticles in 10% Hoagland's medium (DEAE = diethylaminoethyl dextran coated CeO_2; DEX = dextran-coated CeO_2; CM= carboxymethyl dextran-coated CeO_2). Dissolved Ce measured after 24 hours. Data are means with standard deviations in parenthesis.

Nanoparticle treatments	Volume weighted hydrodynamic diameter	Apparent zeta potential	Dissolved Ce in media (%)
DEAE-CeO_2	16 nm (2.3 nm)	+13 mV (0.67 mV)	0.22 (0.07)
DEX-CeO_2	22 nm (3.5 nm)	-3 mV (0.36 mV)	0.31 (0.06)
CM-CeO_2	20 nm (3.8 nm)	-15 mV (1.23 mV)	0.26 (0.04)

Figure 1. Reduction in biomass production for shoots (A) and roots (B) upon treatment with CeO_2 nanoparticles coated with diethylaminoethyl dextran (DEAE, +), dextran (DEX, N) or carboxymethyl dextran (CM, -). Statistical significance detected by post-hoc Tuckey's tests on the coating factor is denoted by * (between treatment groups) and # (treatment vs. control), $p<0.05$ and $p<0.01$ levels are indicated by single and double symbols.

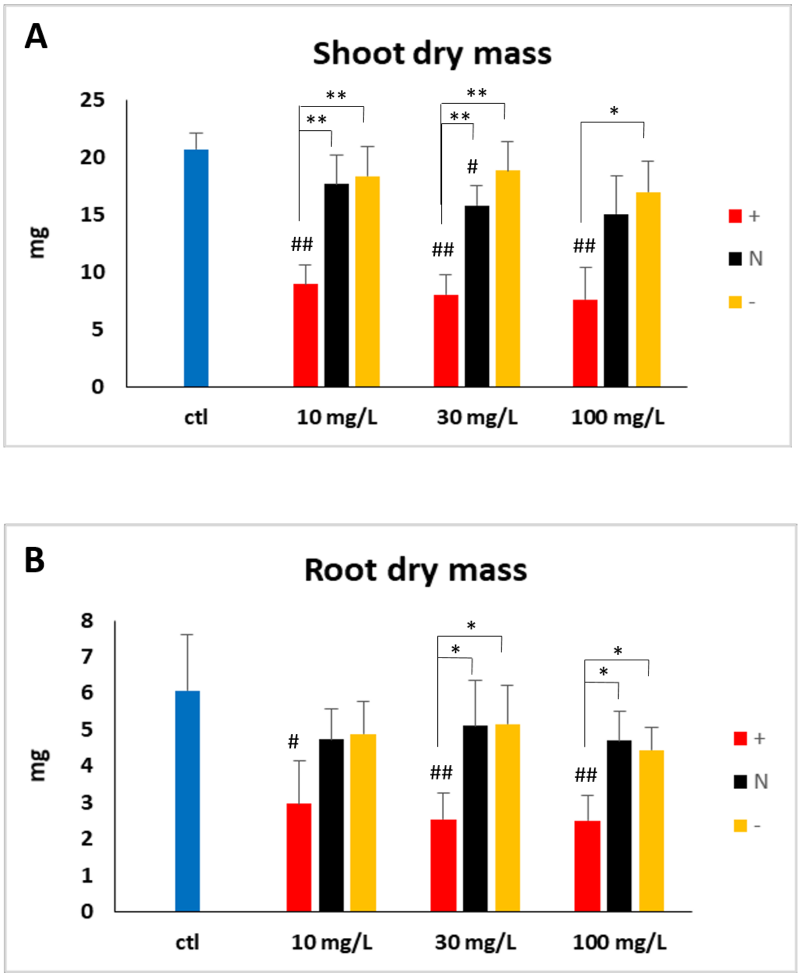

Figure 2. Micrographs showing histological lesions at the root tips. A, control, B, DEAE, C, DEX. Damage to the meristem is pointed out by arrows in B&C. There are extensive cellular abnormalities and void necrotic regions around the meristem. Scale bar = 50 μm.

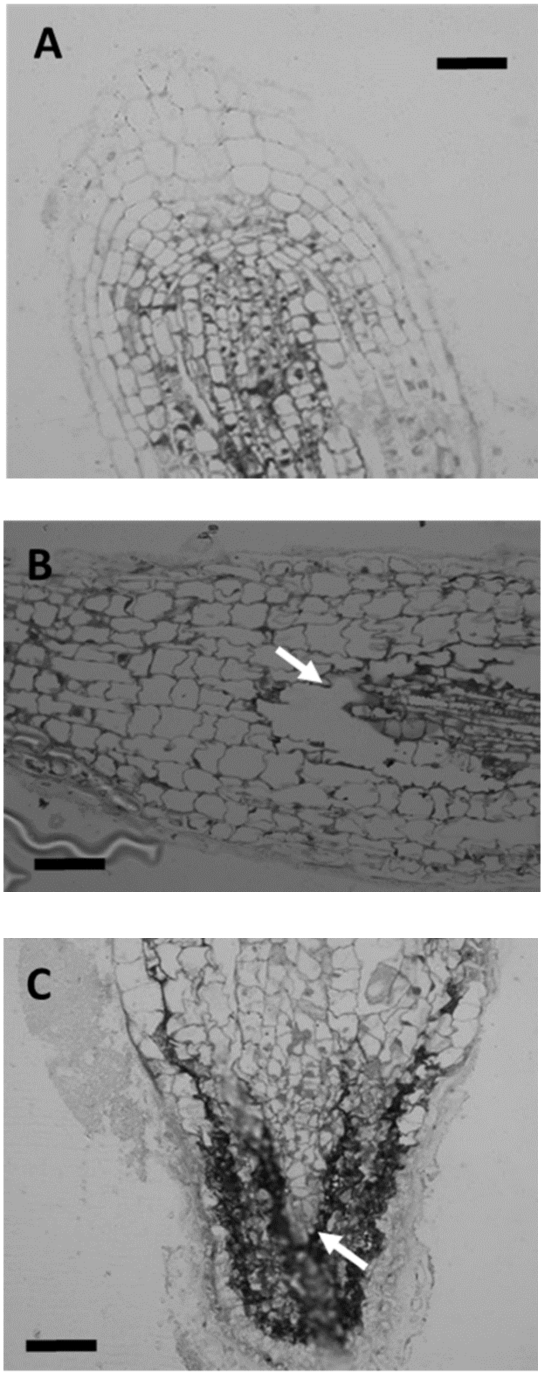

Figure 3. Bulk tissue concentration of Ce in root and shoot was determined for treatment groups DEAE, DEX, and CM after two weeks of treatment. See text for details. The same statistical procedures were used to analyze the data set as in Fig 1. Significant differences detected by post-hoc Tuckey's tests on the coating factor are denoted by * ($p<0.05$) and ** ($p<0.01$).

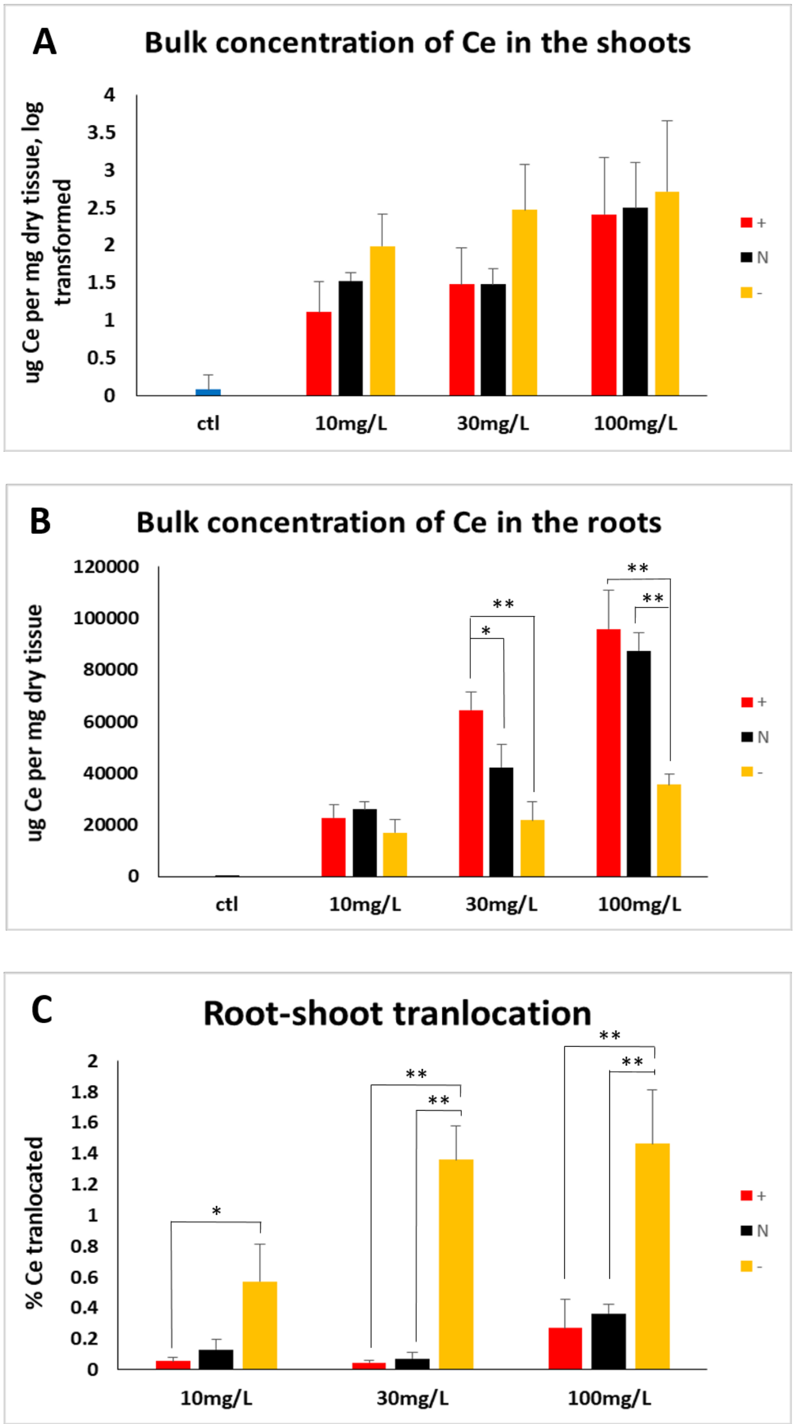

Figure 4. X-ray fluorescence micrographs of root tip cross sections for DEX (A-E), CM (F-J), and DEAE (K-M). B, G, and L are 1 µm resolution coarse maps of Ce distribution throughout the root collected at Advanced Photon Source sector 13. Images C, D, and E represent magnified view of the rectangular regions in B, and were collected at the Hard X-ray nanoprobe (HXN) beamline of the National Synchrotron Light Source II at a 60 nm sampling resolution. Image E is further described in Figure 5. These images show subcellular features near the epidermis, cortex and stele, respectively. Images H, I are 60 nm sampling resolution images of the rectangular regions in G, showing distribution in the cortex and at the endodermis, respectively. The squared region in J was mapped with ultra-high 15 nm resolution (H), showing signs of endocytic transport of Ce (putative vesicular structures indicated by arrows). Image M is a 60 nm resolution image of the rectangular region in L, at the epidermis. A, F and K are light micrographs of the root sections. Scale bars: B,G, and L-50 µm, C,D,G,H and L- 5 □m, E- 2 □m, I- 200 nm. Cy = cytoplasm; Ap = apoplast; Va = vacuole; En = endosome.

(Figure on next page)

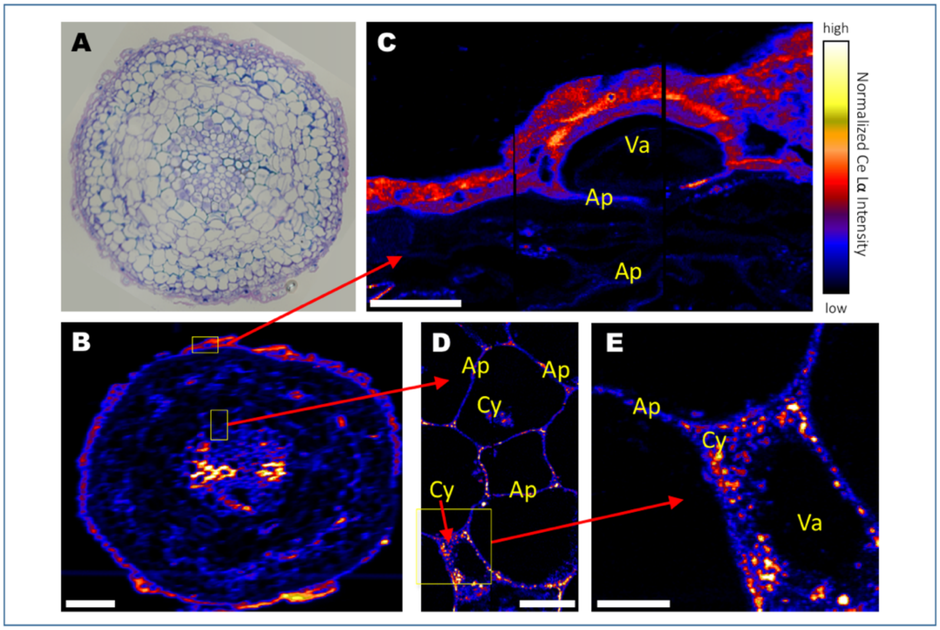
A
C
Va
Ap
Ap
high
Normalized Ce Lα Intensity
low
B
D
Ap
Ap
Cy
Cy
Ap
E
Ap
Cy
Va

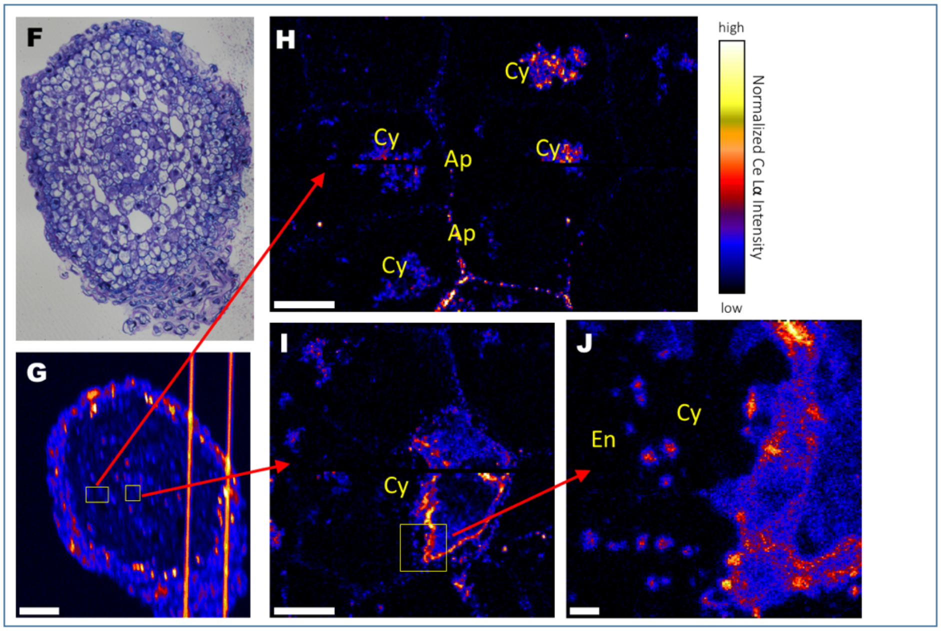
F
H
Cy
Cy
Ap
Cy
Ap
Cy
high
Normalized Ce Lα Intensity
low
G
I
Cy
J
Cy
En

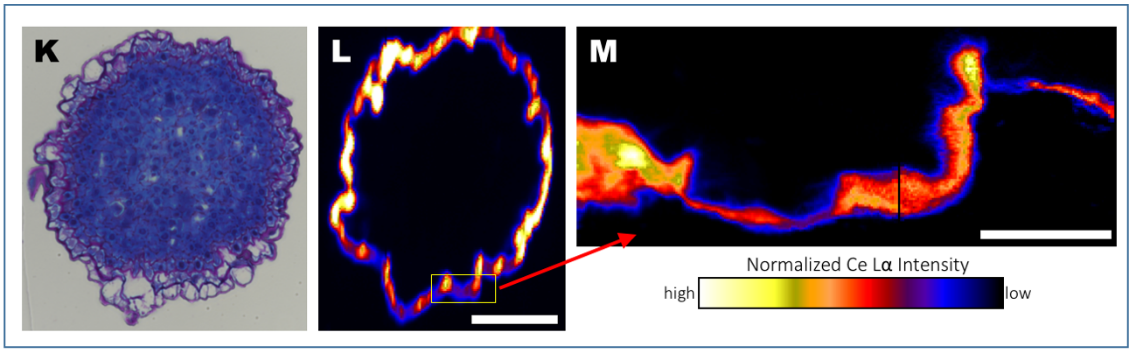
K
L
M
Normalized Ce Lα Intensity
high
low

Figure 5. A 60 nm sampling resolution image collected at NSLS-II from near the stele of the root from a DEX treated plant. Brighter areas indicate areas of increased Ce La fluorescence intensity. Clearly visible in this image is Ce within the apoplast and within endosomes located in the cytoplasm surrounding the vacuole (annotated at the right).

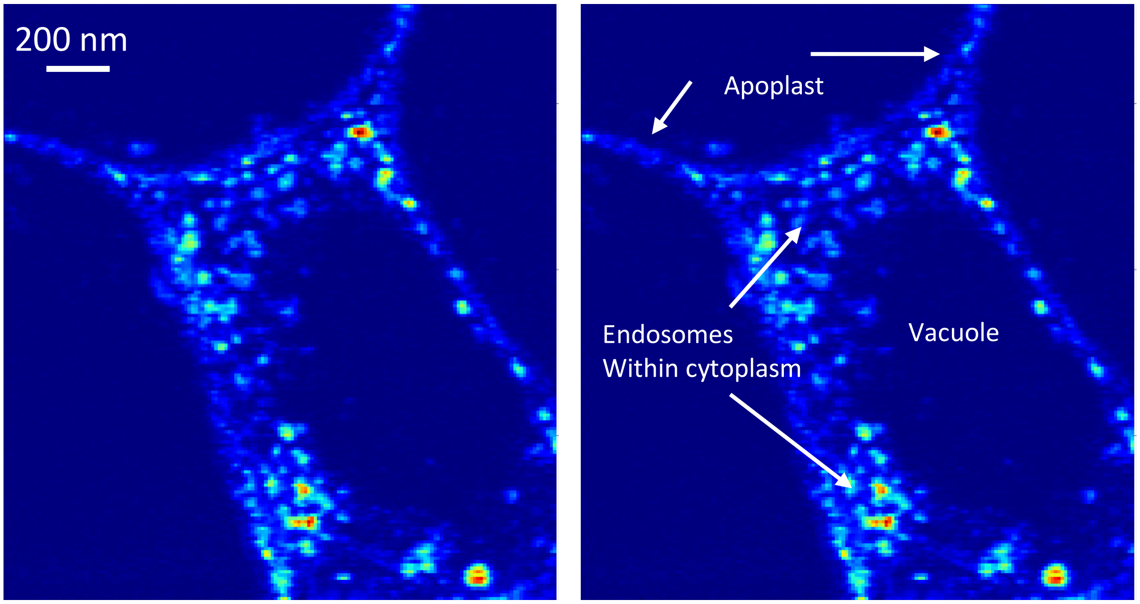

Figure 6. In situ Ce L3-edge XANES spectra of the root cross sections. A-C) Merged spectra from hot spots in different regions of the section. DEAE: #1-12, epithelium; #13, cortex. DEX: #7-8, epithelium; #5,6,9, cortex; #1-4,10, vasculature. CM: #1,2,7-11, epithelium; #3-4, cortex; #5-6, vasculature. D) Linear combination was used to fit the spectra with the two standards. The respective contributions of Ce (III) and Ce (IV) are not forced to sum to 100%. Quality of the fit is denoted by reduced chi-squared. Epi, epithelium; Cor, cortex; Vas, vasculature. Scale bar in the XRF graph = 50 μm. Examples of individual fits are shown in the Fig S5. The horizontal lines in figure C are from scattered X-rays from the platinum grid on the sample holder, not Ce.

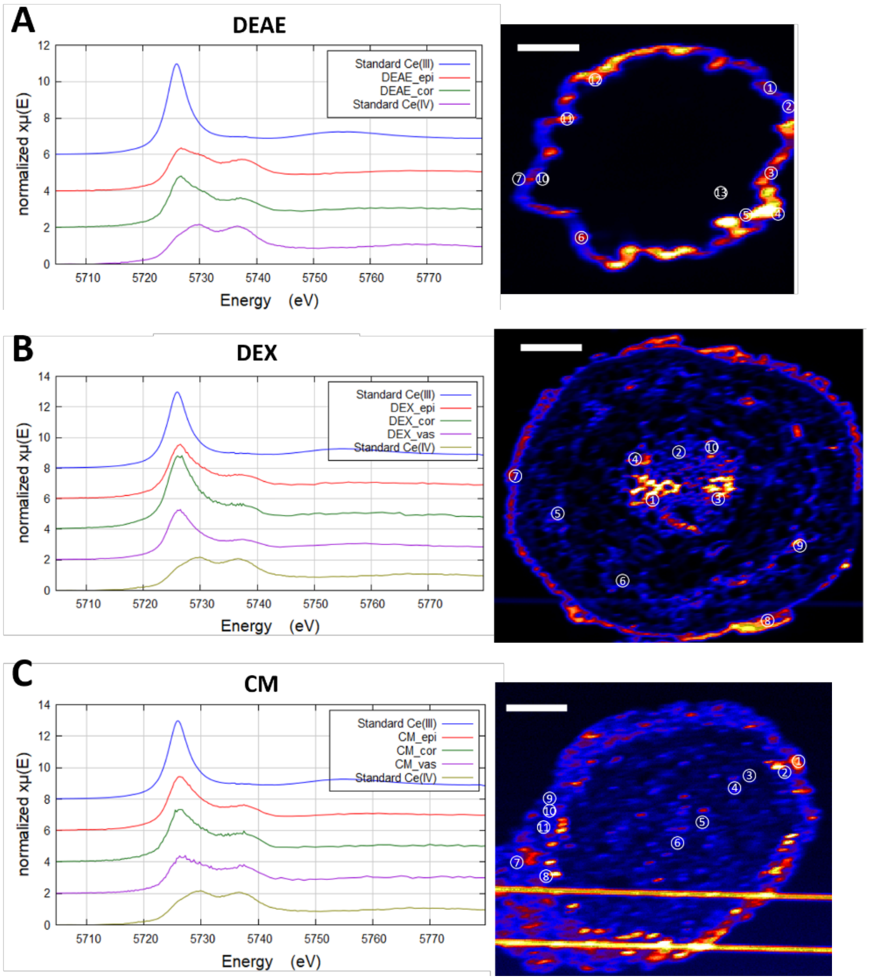

D

Spectrum	CeIII (%)	CeIV (%)	Reduced Chi-squared
DEAE-Epi	22.1	73.5	0.002
DEAE-Cor	34.0	66.9	0.006
DEX-Epi	55.2	46.7	0.016
DEX-Cor	89.0	32.3	0.069
DEX-Vas	55.9	36.1	0.006
CM-Epi	54.2	52.0	0.004
CM-Cor	48.5	63.9	0.007
CM-Vas	24.0	72.1	0.003

Figure 7. XRF scans and in situ Ce L3-edge XANES spectra of the leaf samples from three treatments. A) CM, B) DEX, C) DEAE. Signals of Ce and K are represented in the red and green channel of the images, respectively. Regions from which XANES spectra shown in Fig. 6 were collected are indicated by numbered squares. Scale bar = 20 µm. D) Merged XANES spectra from leaf areas denoted by squares. DEX1 are collected from hotspots within veins (#2,3&6 in Fig.7B), DEX2 from hotspots in the mesophyll (#1,4,5&7 in Fig 7B). E) Linear combination was used to fit the spectra with the two standards. The respective contributions of Ce (III) and Ce (IV) are not forced to sum to 100%. Quality of the fit is denoted by reduced Chi-squared.

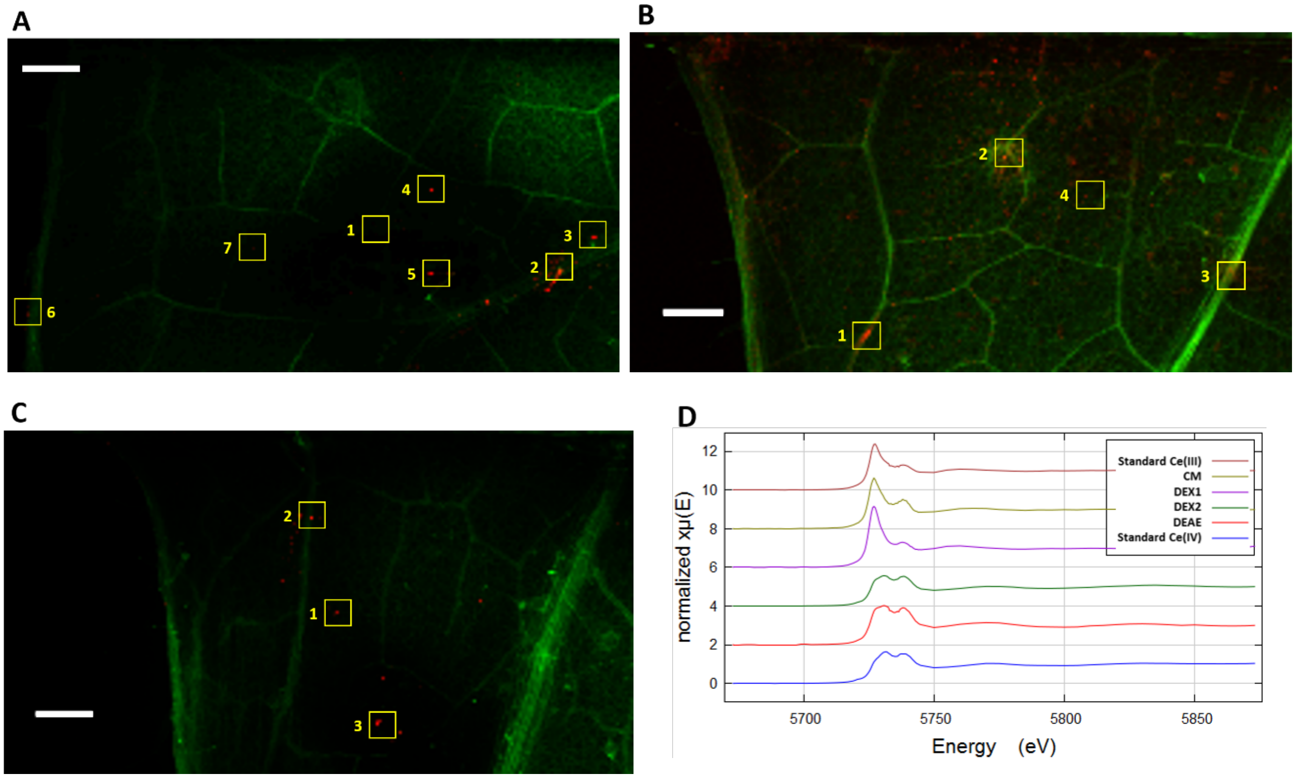

E

Spectrum	CeIII (%)	CeIV (%)	Reduced Chi-squared
DEAE	10.4	88.2	0.004
DEX1	47.9	45.9	0.022
DEX2	4.8	73.8	0.007
CM	37.8	50.8	0.004

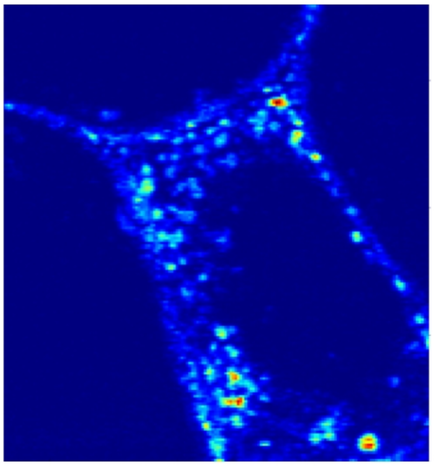

338x190mm (90 x 90 DPI)